

Constructing the frequency and wave normal distribution of whistler-mode wave power

Article

Accepted Version

Watt, C. E. J., Degeling, A. W. and Rankin, R. (2013)
Constructing the frequency and wave normal distribution of
whistler-mode wave power. *Journal of Geophysical Research:
Space Physics*, 118 (5). pp. 1984-1991. ISSN 2169-9402 doi:
<https://doi.org/10.1002/jgra.50231> Available at
<https://centaur.reading.ac.uk/32796/>

It is advisable to refer to the publisher's version if you intend to cite from the work. See [Guidance on citing](#).

Published version at: <http://dx.doi.org/10.1002/jgra.50231>

To link to this article DOI: <http://dx.doi.org/10.1002/jgra.50231>

Publisher: American Geophysical Union

All outputs in CentAUR are protected by Intellectual Property Rights law, including copyright law. Copyright and IPR is retained by the creators or other copyright holders. Terms and conditions for use of this material are defined in the [End User Agreement](#).

www.reading.ac.uk/centaur

CentAUR

Central Archive at the University of Reading

Reading's research outputs online

1 Constructing the frequency and wave normal
2 distribution of whistler-mode wave power

C. E. J. Watt, A. W. Degeling, and R. Rankin

3 Department of Physics, University of Alberta, Edmonton, Alberta, Canada

C. E. J. Watt, Department of Physics, University of Alberta, Edmonton, Alberta, T6G 2G7,
Canada (watt@ualberta.ca)

A. W. Degeling, Department of Physics, University of Alberta, Edmonton, Alberta, T6G 2G7,
Canada (degeling@ualberta.ca)

R. Rankin, Department of Physics, University of Alberta, Edmonton, Alberta, T6G 2G7,
Canada (rrankin@ualberta.ca)

4 **Abstract.** We introduce a new methodology that allows the construc-
5 tion of wave frequency distributions due to growing incoherent whistler-mode
6 waves in the magnetosphere. The technique combines the equations of ge-
7 ometric optics (i.e. raytracing) with the equation of transfer of radiation in
8 an anisotropic lossy medium to obtain spectral energy density as a function
9 of frequency and wavenormal angle. We describe the method in detail, and
10 then demonstrate how it could be used in an idealised magnetosphere dur-
11 ing quiet geomagnetic conditions. For a specific set of plasma conditions, we
12 predict that the wave power peaks off the equator at $\sim 15^\circ$ magnetic lati-
13 tude. The new calculations predict that wave power as a function of frequency
14 can be adequately described using a Gaussian function, but as a function of
15 wavenormal angle, it more closely resembles a skew normal distribution. The
16 technique described in this paper is the first known estimate of the paral-
17 lel and oblique incoherent wave spectrum as a result of growing whistler-mode
18 waves, and provides a means to incorporate self-consistent wave-particle in-
19 teractions in a kinetic model of the magnetosphere over a large volume.

1. Introduction

20 Raytracing of whistler-mode waves through the magnetosphere has promoted further
21 understanding of the propagation of these important waves (e.g. *Inan and Bell* [1977];
22 *Thorne et al.* [1979]; *Church and Thorne* [1983]; *Huang and Goertz* [1983]; *Huang et al.*
23 [1983]; *Chum et al.* [2003]; *Chum and Santolík* [2005]; *Bortnik et al.* [2006, 2007a, b, 2008];
24 *Li et al.* [2008, 2009]; *Bortnik et al.* [2011a]). By combining raytracing and solutions from
25 the linear dispersion relation, the parameters governing the linear behaviour of a wave
26 of frequency $\omega = 2\pi f$ can be diagnosed at each step along the ray path: wavenormal
27 angle, ray direction, group time, linear growth rate and path-integrated gain. The gain of
28 a single wave is not a parameter that is measured by spacecraft, and the wave spectrum
29 at any one point represents the combined gain of many waves with different trajectories
30 and histories. Instead, a more useful quantity is wave energy density as a function of
31 frequency and wavenormal angle, and this is what is often used to drive particle diffusion
32 models (e.g. *Beutier and Boscher* [1995]; *Glauert and Horne* [2005]; *Shprits et al.* [2008];
33 *Su et al.* [2010]).

34 Recent work has sought to construct wave power distributions using ray tracing analysis
35 for damped chorus emissions [*Bortnik et al.*, 2011b; *Chen et al.*, 2012a, b, 2013] and
36 growing incoherent whistler-mode waves [*Watt et al.*, 2012]. The challenge for constructing
37 wave frequency distributions is to include all possible contributions to the wave power from
38 all possible ray paths. The first set of studies invokes the assumption that all wave power
39 is emitted at the magnetic equator, and then the wave power is mapped to different
40 locations using forwards or backwards raytracing, modifying the power to account for

41 geometric effects and Landau damping of the waves [*Bortnik et al.*, 2011b; *Chen et al.*,
42 2012a, b, 2013]. Using a similar method, but with different assumptions, *Watt et al.* [2012]
43 attempted to build up a picture of the incoherent wavepower due to growing whistler-mode
44 waves by tracing tens of millions of raypaths using random initial locations from a region
45 $5 < L < 10$ and $-30^\circ < \lambda < 30^\circ$, and random initial wave parameters selected from the
46 range of unstable frequencies and wave normal angles. The key difference between the
47 two approaches is that *Watt et al.* [2012] make no assumptions regarding source location;
48 waves may be generated anywhere in the magnetosphere where the local plasma conditions
49 support linear whistler-mode wave growth. Nonetheless, the approach of *Watt et al.* [2012]
50 only yields the distribution of wave gain at any particular location. Distributions of wave
51 gain can provide some indication of the wave parameters that encourage the most growth,
52 but cannot be compared directly with satellite observations.

53 In this paper we describe a technique that estimates spectral energy density from these
54 gains as a function of frequency and wavenormal angle. Our aim here is to elucidate how
55 to construct the wave frequency distributions for growing incoherent waves; future work
56 will use the technique to investigate wave distributions throughout the magnetosphere for
57 different conditions, and investigate the effects that these self-consistent wave distributions
58 have on the resulting electron diffusion.

59 In section 2, we describe how raytracing and path-integrated gain calculations may be
60 used to construct wave frequency distributions in the magnetosphere. Section 3 presents
61 an example of wave frequency distributions during quiet times as a function of latitude
62 in the model. Examples of wave normal distributions are presented in Section 4. We

63 discuss possible uses of these calculations in Section 5, before presenting our conclusions
 64 in Section 6.

2. From raytracing to spectral energy density

65 The spectral energy density of waves u_ω in an arbitrary anisotropic medium may be
 66 calculated from:

$$67 \quad u_\omega = \int_{4\pi} \frac{I_\omega}{v_g} d\chi \quad (1)$$

68 where u_ω is measured in joules per cubic metre per frequency interval $d\omega$, I_ω is the intensity
 69 of the radiation, v_g is the local group velocity of waves of that frequency, and χ is the
 70 angle of the group velocity relative to the magnetic field, or ray direction. In this case, we
 71 will measure χ relative to the local magnetic field (i.e. χ is the angle between \mathbf{v}_g and \mathbf{B}_0).
 72 Note that for the demonstration in this paper, we will ignore any azimuthal propagation
 73 of the whistler-mode waves, and so the integration in equation [1] will cover 2π , although
 74 it will be straightforward to extend the calculation to three dimensions where χ is a solid
 75 angle. The calculation of spectral energy density therefore requires us to find I_ω as a
 76 function of group velocity angle. *Watt et al.* [2012] demonstrated that growing incoherent
 77 whistler-mode waves in a dipolar magnetic field have group velocity angles close to the
 78 anti-parallel and parallel directions (i.e. $\chi < 10^\circ$). Note, however, that the maximum
 79 gains did not occur for propagation that was exactly aligned with the magnetic field, as
 80 is expected from local solutions to the dispersion relation.

81 In an isotropic medium with no emission, absorption or scattering, the ratio I_ω/n^2 is
 82 constant along a ray path, where $n = |\mathbf{n}| = |c\mathbf{k}/\omega|$ is the refractive index of the medium.
 83 The appropriate generalisation of this ratio for an anisotropic medium is that I_ω/n_r^2 is

constant, where n_r is the "ray refractive index" of the medium given by *Bekefi* [1966]:

$$n_r^2 = \left| n^2 \sin \psi \frac{(1 + \nu^2)^{1/2}}{\frac{\partial}{\partial \psi} \left(\frac{\cos \psi + \nu \sin \psi}{(1 + \nu^2)^{1/2}} \right)} \right| \quad (2)$$

Here, ψ is wavenormal angle (i.e. the angle between \mathbf{k} and \mathbf{B}_0), and $\nu = (1/n)(\partial n/\partial \psi)_\omega$.

By including growth or damping of waves due to interactions with the plasma, the change in I_ω/n_r^2 along the raypath can be written (c.f. *Church and Thorne* [1983]):

$$\frac{d}{ds} \left(\frac{I_\omega}{n_r^2} \right) = 2 \frac{\omega_i}{v_g} \cos \alpha \frac{I_\omega}{n_r^2} \quad (3)$$

where ω_i is the imaginary frequency of the wave and α is the angle between the group velocity vector and the wavenumber vector. The solution to equation [3] gives the value of intensity at point b along the raypath s :

$$\frac{I_\omega(b)}{n_r^2(b)} = \frac{I_\omega(a)}{n_r^2(a)} \exp \left[\int_a^b 2 \frac{\omega_i(s)}{v_g(s)} \cos(\alpha(s)) ds \right] \quad (4)$$

Note that the integral in equation [4] is equivalent to the calculation of path-integrated gain between points a and b ,

$$\Gamma(a, b) = \int_a^b -k_i \cos \alpha ds = \int_a^b \frac{\omega_i(s)}{v_g(s)} \cos(\alpha(s)) ds, \quad (5)$$

c. f. *Horne and Thorne* [1997] and *Watt et al.* [2012] (and note that the factor of 8.6859 required to convert gain to dB is not required in these calculations). To evaluate the integral in equation [1], we must now find all the intensity contributions from all waves passing through location b .

We will demonstrate our calculations using the same magnetic field and plasma model used by *Watt et al.* [2012]. This study used data from the THEMIS spacecraft published by *Li et al.* [2010] to constrain the choice of plasma parameters. Again, in this paper, we will focus on quiet times ($AE < 100$ nT), and on observations taken outside the plasmasphere at 9MLT as an example of a location where whistler-mode waves are observed.

106 We construct an idealised dipole model of the magnetospheric magnetic field between
 107 $L = 5$ and $L = 10$. A modified diffusive equilibrium model for the electron number density
 108 N_e [*Inan and Bell, 1977*], similar to models used by *Bortnik et al.* [2006, 2007a, b, 2011a],
 109 is used, with parameters chosen to fit the density profiles shown in *Li et al.* [2010]. The
 110 model, and the parameters chosen, are discussed in detail in the Appendix of *Watt et al.*
 111 [2012] and are shown to produce values of $N_e(L)$, and hence the ratio of plasma frequency
 112 to gyrofrequency ω_{pe}/Ω_e that matches the variation observed in the statistical THEMIS
 113 measurements (see Figure 1b of *Li et al.* [2010]).

114 The choice of distribution of warm/hot electrons which provide the plasma instability
 115 is also guided by observations provided in *Li et al.* [2010]. It was found that two warm
 116 plasma components, one with $T_{\parallel} = 1.4\text{keV}$ and one with $T_{\parallel} = 10\text{keV}$ could be used
 117 to provide a reasonable fit to the THEMIS survey parameters. Simple functional forms
 118 for number density and temperature anisotropy were derived in *Watt et al.* [2012] that
 119 describe the variation of these parameters with L . The functions adequately reproduced
 120 the statistical survey of anisotropy and phase space density. If $w = (r_{eq}/R_E) - 5$, and r_{eq}
 121 is the radial distance at the equator, then the functional forms for populations 1 and 2 in
 122 the equatorial plane are:

$$123 \quad A_{\text{eq},1} = 0.004w^3 + 0.2w \quad (6)$$

$$124 \quad A_{\text{eq},2} = 0.0061w^3 \quad (7)$$

$$125 \quad n_{\text{eq},1} = 10^5 + 3.0 \times 10^5 w \quad (8)$$

$$126 \quad n_{\text{eq},2} = 5.0 \times 10^4 - 8.0 \times 10^3 w \quad (9)$$

127 The cold plasma density is set equal to $N_e - n_{\text{eq},1} - n_{\text{eq},2}$. The free energy driving the
 128 unstable growth of the waves is therefore an electron temperature anisotropy at large
 129 values of L .

130 Figure 1a shows a growing raypath arbitrarily selected from one of the millions of
 131 raypaths used in the analysis of *Watt et al.* [2012]. We follow this raypath only for
 132 demonstration purposes, before describing later how raypaths will be specially selected
 133 to build up the wave distributions. The raypath follows waves with real frequency $f =$
 134 $\omega/(2\pi) = 200$ Hz and initial wavenormal angle $\psi_0 = -11^\circ$ from the initial point at a radial
 135 distance $r = 9R_E$ and magnetic latitude $\lambda = -6^\circ$ (indicated by the solid green square).
 136 Assuming no azimuthal propagation, the ray path (solid black line) travels northwards
 137 towards the equator and passes into the northern hemisphere, where it is stopped at
 138 an arbitrary location for this demonstration. The arrow on the raypath indicates the
 139 ray direction. Indicated with coloured dots are locations along the trajectory where the
 140 growth rate is positive; warm colours indicate larger growth rates than cooler colours.
 141 Figure 1b shows these growth rates as a function of distance s along the path. Growth
 142 rates are only positive near the beginning of the raypath, and it is only at these locations
 143 that waves can be generated. Imagine an "observation location" along the raypath, where
 144 we might wish to construct a wave frequency distribution (indicated with the open black
 145 square). The contributions to the wave energy density at $f = 200$ Hz at this location will
 146 depend upon how many waves arrive at this location, and their path-integrated gain. We
 147 calculate the individual $\Gamma(a, b)$ contributions by letting a run through all the points where
 148 $\omega_i > 0$ along the path, and setting b equal to the value of s at the observation location. The
 149 black dots in Figure 1d show these $\Gamma(a, b)$ contributions. Note that the largest gains are

150 contributed by waves that have travelled furthest to arrive at the observation point (i.e.
 151 from those waves that started near $s = 0$). Waves that started too near the observation
 152 point have negative gain, because they are mostly damped; they will not contribute to u_ω
 153 at this frequency. The total contribution from the sum of all incoherent waves generated
 154 along this raypath from the arbitrary start point s_0 to the selected observation point is
 155 therefore:

$$156 \quad \mathcal{I}(b) = I_0 n_k^2(b) \int_{s_0}^{s_1} \frac{\exp(\Gamma(s, b))}{n_k^2(s)} ds \quad (10)$$

157 where it is assumed that all waves have the same initial intensity I_0 , and s_1 is the last
 158 point along the raypath with $\omega_i > 0$ and $\Gamma > 0$.

159 By choosing an observation point further from the initial point (e.g. the red square in
 160 Figure 1a), we can see that there are no contributions to u_ω from any point along the
 161 path where $\omega_i > 0$. All values of Γ shown by red dots in Figure 1d are negative.

162 The arbitrary initialisation point used in the traditional forward raytracing displayed
 163 in Figure 1a is not the best selection for s_0 in equation [10] and the subsequent raypath is
 164 not guaranteed to include all possible contributions from waves along that raypath; there
 165 could be points further from the observation point that also have $\omega_i > 0$ and give $\Gamma > 0$.
 166 The best way to include all possible contributions, and therefore establish s_0 and s_1 along
 167 each path, is to trace rays *backwards* from the observation point. Figure 2 demonstrates
 168 how s_0 and s_1 can be chosen using backwards raytracing. The same raypath shown in
 169 Figure 1 is traced backward from the observation location (open black square). Figure 2b
 170 shows the growth rates calculated along the path, where $s = 0$ indicates the observation
 171 location. Only at those points with $\omega_i > 0$ (indicated by the black curve) will waves grow,
 172 waves are damped elsewhere (grey curves). The path-integrated gain between each point

173 and the observation point is also calculated (shown in Figure 2c). The black dots indicate
 174 those potential ray start-points where waves will grow *and* contribute a positive gain at
 175 the observation point. The values of s_0 and s_1 can easily be obtained by applying these
 176 two conditions.

177 Equation [1] shows that we must find all raypaths that pass through an observation
 178 point at each frequency. We sweep through the wavenormal angle ψ , backtracing rays
 179 of constant ω from the observation point to high latitudes. *Watt et al.* [2012] showed
 180 that for these plasma conditions, growing paths are confined to $\lambda \pm 30^\circ$ and so backward
 181 raypaths are ended once they reach $\lambda \pm 40^\circ$. The process shown in Figure 2 is repeated for
 182 each raypath. Some raypaths have no regions of $\omega_i > 0$ and are ignored. Figure 3a shows
 183 the colour-coded contributions to the intensity $\mathcal{I}(b)$ for $f = 200$ Hz at an observation point
 184 6° south of the equator, calculated using this backwards ray-tracing algorithm. A number
 185 of raypaths are shown to contribute to u_ω , with different wavenormals and ray directions
 186 at the observation point. The contribution to wave intensity from each path is given by
 187 equation [10], and is shown in Figure 3b and c as a function of χ , measured clockwise from
 188 the magnetic field direction. We will display angles in degrees rather than radians as the
 189 angles are quite small. The intensity peaks near the parallel and anti-parallel directions,
 190 but not directly along the field. It is a simple matter to numerically integrate $\mathcal{I}(\chi)$ as
 191 shown in Figure 3b and c to obtain u_ω for $f = 200$ Hz.

192 Figure 4 shows the spectral energy density (normalised to the initial wave intensity I_0)
 193 calculated using the backward raytracing technique as a function of normalised frequency
 194 at $r = 9R_E$ and $\lambda = -6^\circ$ (the observation point indicated in Figure 3a). It is important to
 195 note that the inputs for this model are the form of the magnetic field and the variation in

196 the cold and warm plasma; the waves grow self-consistently according to the free energy
 197 in the plasma. For this specific set of conditions, the wave spectra is narrowly peaked
 198 at $f = 200$ Hz and drops off quickly at higher and lower frequencies. Given that all the
 199 waves have the same initial intensity I_0 , regardless of frequency or wavenormal angle, it
 200 is very interesting to discover that as a function of frequency only, our prediction of u_ω at
 201 this low latitude can be approximated using a Gaussian function:

$$202 \quad u_\omega \approx A \exp \left[- \left(\frac{(\omega/\Omega_e) - \omega_m}{\delta\omega} \right)^2 \right] \quad (11)$$

203 where $\omega_m = 0.165$ and $\delta\omega = 0.051$ (indicated by the solid line in Figure 4). It is im-
 204 portant to note that the approximately Gaussian distribution of waves near the equator
 205 arises naturally from the calculations, and is not imposed by active manipulation of wave
 206 intensity. We repeat that the only input to the calculations are the choice of plasma
 207 model and magnetic field model. Future work will determine whether the functional form
 208 of the wave distribution near the equator is a natural consequence of the whistler-mode
 209 wave instability, or whether it is controlled by the choice of warm plasma model, or the
 210 latitudinal symmetry of the magnetic field model used in the calculations.

3. Wave frequency distributions as a function of latitude

211 The creation of wave spectra using the backward raytracing allows us to make a pre-
 212 diction of the relative wave power at different latitudes. Figure 5 shows the predicted
 213 variation of wave spectral energy density as a function of magnetic latitude λ at $L = 9$,
 214 using the quiet time plasma model described in *Watt et al.* [2012]. The wave power
 215 increases from the equator to peak at $\lambda \sim 15^\circ$, before dropping off rapidly at higher
 216 latitudes. Near the equator, the wave spectra are approximately Gaussian, but these

217 spectra become more skewed towards lower normalised frequency at higher latitude. Note
 218 that the wave frequencies are normalised to the *local* electron gyrofrequency and the local
 219 gyrofrequency increases with latitude.

4. Wave normal distributions

220 Figure 6 shows the distribution of normalised wave intensity as a function of wavenor-
 221 mal angle and normalised frequency at the equator at $L = 9$ using the same quiet time
 222 plasma model as before. (The dark blue colour in Figure 6a and b corresponding to
 223 $u_{\omega,\psi}/I_0 = \mathcal{I}/(v_g I_O) = 0$ is an artefact of the interpolation software used to make the
 224 surface plot). In agreement with the forward raytracing results of *Watt et al.* [2012], the
 225 maximum wave intensity occurs for oblique wavevectors, even at the equator. Figure 6c
 226 and d show slices through these distributions at constant frequency. The wave intensity
 227 distribution is exactly symmetric about $\psi = 90^\circ$ (or $\pi/2$) and more closely resembles a
 228 skew normal distribution [*O'Hagan and Leonard, 1976*] than a Gaussian distribution. It
 229 is important to note that our method predicts that wave power near to the equator is a
 230 combination of waves travelling in opposite directions. The wavenormal distribution peaks
 231 at $\sim 12^\circ$ and $\sim 168^\circ$, where ψ is measured clockwise from the magnetic field direction.

232 At $\lambda = 15^\circ$ magnetic latitude, the wavenormal distribution has become much less sym-
 233 metric and peaks at a slightly higher wavenormal angle. Figure 7 shows that the intensity
 234 peaks at around $\psi \sim 20^\circ$, and that there is very little wave power with wavenormals
 235 pointing towards the equator.

5. Discussion

236 Predictions of the pitch-angle and energy diffusion due to interactions with whistler-
 237 mode waves are a vital part of many models of the Earth's radiation belts. Most models
 238 incorporate a set of quasilinear diffusion coefficients which are driven by prescribed wave
 239 distribution functions as first suggested by *Lyons et al.* [1971]. Many state-of-the-art
 240 physics-based models of radiation belt diffusion use this method, e.g. the Salammbô code
 241 [*Beutier and Boscher, 1995*]), the Pitch Angle and Energy Diffusion of Ions and Elec-
 242 trons code (PADIE, *Glauert and Horne* [2005]), the Versatile Electron Radiation Belt
 243 code (VERB, *Shprits et al.* [2008]), and the Storm-Time Evolution of Electron Radiation
 244 Belt code (STEERB, *Su et al.* [2010]). Commonly, the prescribed wave distribution func-
 245 tion is separated into two independent Gaussian functions dependent on frequency and
 246 wavenormal angle (e.g., *Glauert and Horne* [2005]):

$$247 B^2(\omega) = \begin{cases} A^2 \exp\left(-\frac{(\omega-\omega_m)^2}{\delta\omega^2}\right), & \text{if } \omega_{lc} < \omega < \omega_{uc} \\ 0, & \text{otherwise} \end{cases} \quad (12)$$

$$248 g(X) = \begin{cases} \exp\left(-\frac{(X-X_m)^2}{X_w^2}\right), & \text{if } X_{min} < X < X_{max} \\ 0, & \text{otherwise} \end{cases} \quad (13)$$

249 where ω_m is the frequency of maximum wavepower, $\delta\omega$ is the frequency width, ω_{lc} , ω_{uc}
 250 are the lower and upper frequency cutoffs, $A^2(\omega, \omega_m, \omega_{lc}, \omega_{uc})$ is a normalisation constant,
 251 $X = \tan \psi$, X_m is the value of X corresponding to maximum wavepower, X_w is the
 252 width, and X_{min} , X_{max} are the minimum and maximum values of X . The separation
 253 of variables in these functions allows for significant mathematical simplification of the
 254 calculation of the diffusion coefficients, but is not motivated by observations; the exact
 255 functional form of $\mathbf{B}^2(\omega, \psi)$ is unknown. Figures 6 and 7 show predictions of this function
 256 from a combination of raytracing and solutions to the linear dispersion relation. Although
 257 the variation of u_ω with frequency is approximately Gaussian near the equator, at higher

latitudes it more closely resembles a skew normal function [O'Hagan and Leonard, 1976].
The variation of $u_{\omega,\psi}$ with ψ resembles a skew normal function at all latitudes. Future
work will determine whether $u_{\omega,\psi}$ can be best described using two independent functions
of ω and ψ or whether the relationship is more complicated.

Quantitative predictions of the wave spectral energy density require an estimate of the
original intensity of the waves I_0 . In the absence of other plasma instabilities, the initial
intensity of each wave is likely related to the amplitude of the thermal noise in the plasma
(see e.g. Fejer and Kan [1969]), and this may vary with frequency and wavenumber.
In an inhomogeneous magnetic field, the thermal noise is difficult to calculate from first
principles, and so we leave an estimate of I_0 to future work. A more realistic alternative
is to validate the predicted wave distributions using *in-situ* observations of incoherent
whistler-mode waves. In this way, the initial wave intensity may be calibrated.

An important assumption inherent in the characterisation of the wave distributions
above (equations [12] and [13]) is that the wave distributions are symmetric with respect
to $\pm k_{\parallel}$, or around $\psi = \pi/2$ (see Appendix B, Lyons *et al.* [1971]). The linear prediction
provided by our raytracing analysis predicts such symmetry only at the equator; at higher
latitudes, the wave distributions are skewed in the direction away from the equator.

This study has been constructed using a quiet time plasma model (see Li *et al.* [2010]
and Watt *et al.* [2012]). Because quiet time parameters were used, wave growth is limited
to large values of L . There are many variables in these plasma models, including the
choice of the number of warm plasma components, and their variations in temperature,
anisotropy and density. It is likely that the predicted wave distributions will be sensitive to
these choices, but it is important to base those choices on observations. Surveys like those

281 published by *Li et al.* [2010] are therefore indispensable. Investigations of the sensitivity
282 of the predicted wave distributions to the plasma parameters chosen is a formidable task,
283 given the number of parameters involved, and will be reported in future work.

284 An interesting alternate raytracing technique is presented in *Chen et al.* [2013] to study
285 the power spectra of whistler-mode waves, specifically lightly-damped chorus waves. The
286 method presented by *Chen et al.* [2013] uses a prescribed source distribution of waves at
287 the magnetic equator, and predicts the wave spectra that result as the source waves are
288 damped in their passage through the magnetosphere. The calculations presented in this
289 paper are a method to predict the spectra of growing incoherent whistler-mode waves
290 with no constraints placed on the original intensity or source of the waves. Both methods
291 are non-local, and follow waves with different characteristics as they move independently
292 in both radial and latitudinal directions along different paths. The methods presented in
293 *Chen et al.* [2013] and in this article are complementary, and provide useful methods to
294 track whistler-mode wave activity through the magnetosphere.

295 The technique we have described can be used to make predictions of the wave distri-
296 butions at any location, as long as the generated waves obey the caveats of quasilinear
297 theory, i.e. they are incoherent and broadband, and have amplitudes that result in small
298 perturbations in the plasma distribution function. The technique used in this paper can-
299 not predict the wave distributions of whistler-mode chorus waves, since they most likely
300 have a nonlinear generation mechanism [*Katoh and Omura*, 2007; *Omura et al.*, 2008;
301 *Hikishima et al.*, 2009; *Katoh and Omura*, 2011]. These calculations are more relevant for
302 prediction of the amplitude of "hiss-like" whistler-mode waves, similar to those observed
303 and characterised in the equatorial plane by *Li et al.* [2012]. The backwards raytracing

304 technique can be used to predict the wave distributions of other types of electromagnetic
305 wave that exhibit "ray" behaviour and that are driven unstable by a relatively simple
306 instability (e.g. anisotropy driven electromagnetic ion cyclotron waves) and so has more
307 general utility.

308 To obtain a prediction of the wave distribution, the plasma must be modelled not just
309 at the observation location, but in a volume of space surrounding the observation location
310 that could support whistler-mode waves. Observational studies are required to constrain
311 the energetic plasma components that contribute to wave growth (e.g. number density,
312 temperature, anisotropy). For example, it is unclear whether the simple model of warm
313 plasma parameters as a function of latitude used in this paper and in *Watt et al.* [2012]
314 is adequate for modelling the magnetosphere. Given observational surveys of energetic
315 plasma over large regions of the magnetosphere, our new model can be validated with *in*
316 *situ* observations of incoherent whistler-mode waves in different locations. Furthermore,
317 the backwards raytracing approach described in this paper offers the first step to con-
318 structing self-consistent kinetic models of whistler-mode wave-particle interactions over a
319 large volume of the magnetosphere, where the balance between wave growth and particle
320 diffusion could be studied more realistically.

6. Conclusion

321 In this paper we have have introduced a methodology to construct the distribution of
322 incoherent growing whistler-mode waves numerically from a combination of raytracing
323 and solutions to the linear dispersion relation. We describe how to combine the equations
324 of radiation and geometric optics to predict all of the contributions to wave power at any
325 particular location as a function of frequency and wavenormal angle. To demonstrate

326 the capability of the technique, we show that in an idealised quiet-time magnetosphere
327 at 9MLT and $L = 9$, the wave power peaks off the equator at 15° magnetic latitude.
328 The wave spectral energy density can be approximated reasonably well with a Gaussian
329 function, but the wavenormal distribution is best described by a skew normal distribution
330 in wavenormal angle ψ , and most power lies in the wavenormals pointing away from the
331 equator. The wave power does not peak at $\psi = 0, \pi$ (even at the equator), but at a small
332 oblique angle that increases with latitude.

333 As far as we are aware, this is the first time a methodology has been presented that
334 allows the parallel and oblique incoherent wave spectrum to be calculated due to growing
335 whistler-mode waves. It provides a means by which electron diffusion models can be
336 made more self-consistent, by predicting the wave distributions as a function of plasma
337 conditions, without having to run prohibitively-expensive kinetic simulations.

338 **Acknowledgments.** CEJW and AWD are supported by the Canadian Space Agency
339 and NSERC, the Natural Science and Engineering Council of Canada.

References

- 340 Bekefi, G. (1966), *Radiation Processes in Plasmas*, 377 pp., John Wiley and Sons, Inc.,
341 New York, NY, U.S.A.
- 342 Beutier, T., and D. Boscher (1995), A three-dimensional analysis of the electron radiation
343 belt by the Salammb code, *Journal of Geophysical Research*, *100*, 14,853–14,861.
- 344 Bortnik, J., U. S. Inan, and T. F. Bell (2006), Landau damping and resultant unidi-
345 rectional propagation of chorus waves, *Geophysical Research Letters*, *33*, L03102, doi:
346 10.1029/2005GL024553.

- 347 Bortnik, J., R. M. Thorne, and N. P. Meredith (2007a), Modeling the propagation char-
348 acteristics of chorus using CRRES suprathermal electron fluxes, *Journal of Geophysical*
349 *Research*, *112*, A08204, doi:10.1029/2006JA012237.
- 350 Bortnik, J., R. M. Thorne, N. P. Meredith, and O. Santolík (2007b), Ray tracing of
351 penetrating chorus and its implications for the radiation belts, *Geophysical Research*
352 *Letters*, *34*(15), L15109, doi:10.1029/2007GL030040.
- 353 Bortnik, J., R. M. Thorne, and N. P. Meredith (2008), The unexpected origin of plasma-
354 spheric hiss from discrete chorus emissions, *Nature*, *452*(7183), 62–66.
- 355 Bortnik, J., L. Chen, W. Li, R. M. Thorne, and R. B. Horne (2011a), Modeling the
356 evolution of chorus waves into plasmaspheric hiss, *Journal of Geophysical Research*,
357 *116*, A08221, doi:10.1029/2011JA016499.
- 358 Bortnik, J., L. Chen, W. Li, R. M. Thorne, N. P. Meredith, and R. B. Horne (2011b),
359 Modeling the wave power distribution and characteristics of plasmaspheric hiss, *Journal*
360 *of Geophysical Research*, *116*, A12209, doi:10.1029/2011JA016862.
- 361 Chen, L., J. Bortnik, W. Li, R. M. Thorne, and R. B. Horne (2012a), Modeling the
362 properties of plasmaspheric hiss: 1. Dependence on chorus wave emission, *Journal of*
363 *Geophysical Research*, *117*, A05201, doi:10.1029/2011JA017201.
- 364 Chen, L., J. Bortnik, W. Li, R. M. Thorne, and R. B. Horne (2012b), Modeling the
365 properties of plasmaspheric hiss: 2. Dependence on the plasma density distribution,
366 *Journal of Geophysical Research*, *117*, A05202, doi:10.1029/2011JA017202.
- 367 Chen, L., R. M. Thorne, W. Li, and J. Bortnik (2013), Modeling the Wave Normal Distri-
368 bution of Chorus Waves, *Journal of Geophysical Research*, doi:10.1029/2012JA018343,
369 in press.

- 370 Chum, J., and O. Santolík (2005), Propagation of whistler-mode chorus to low altitudes:
371 divergent ray trajectories and ground accessibility, *Annales Geophysicae*, *23*(12), 3727–
372 3738.
- 373 Chum, J., F. Jiricek, J. Smilauer, and D. Shkyar (2003), Magion 5 observations of chorus-
374 like emissions and their propagation features as inferred from ray-tracing simulation,
375 *Annales Geophysicae*, *21*(12), 2293–2302.
- 376 Church, S. R., and R. M. Thorne (1983), On the origin of plasmaspheric hiss - Ray path
377 integrated amplification, *Journal of Geophysical Research*, *88*, 7941–7957.
- 378 Fejer, J. A., and J. R. Kan (1969), Noise Spectrum Received by an Antenna in a Plasma,
379 *Radio Science*, *4*, 721728.
- 380 Glauert, S. A., and R. B. Horne (2005), Calculation of pitch angle and energy diffusion
381 coefficients with the PADIE code, *Journal of Geophysical Research*, *110*, A04206 doi:
382 10.1029/2004JA010851.
- 383 Hikishima, M., S. Yagitani, Y. Omura, and I. Nagano (2009), Full particle simulation
384 of whistler-mode rising chorus emissions in the magnetosphere, *Journal of Geophysical*
385 *Research*, *114*, A01203, doi:10.1029/2008JA013625.
- 386 Horne, R. B., and R. M. Thorne (1997), Wave heating of He⁺ by electromagnetic ion
387 cyclotron waves in the magnetosphere; Heating near the H⁺-He⁺ bi-ion resonance fre-
388 quency, *Journal of Geophysical Research*, *102*, 11457–11471.
- 389 Huang, C. Y., and C. K. Goertz (1983), Ray-tracing studies and path-integrated gains of
390 ELF unducted whistler mode waves in the earths magnetosphere, *Journal of Geophysical*
391 *Research*, *88*, 6181–6187.

- 392 Huang, C. Y., C. K. Goertz, and R. R. Anderson (1983), A theoretical-study of plasmas-
393 pheric hiss generation, *Journal of Geophysical Research*, *88*, 7927–7940.
- 394 Inan, U. S., and T. F. Bell (1977), Plasmopause as a VLF wave guide, *Journal of Geo-*
395 *physical Research*, *82*, 2819–2827.
- 396 Katoh, Y., and Y. Omura (2007), Computer simulation of chorus wave generation in the
397 Earth’s inner magnetosphere, *Geophysical Research Letters*, *34*(3), L03102.
- 398 Katoh, Y., and Y. Omura (2011), Amplitude dependence of frequency sweep rates of
399 whistler-mode chorus emissions, *Journal of Geophysical Research*, *116*, A07201, doi:
400 10.1029/2011JA016496.
- 401 Li, W., R. M. Thorne, N. P. Meredith, R. B. Horne, J. Bortnik, Y. Y. Shprits,
402 and B. Ni (2008), Evaluation of whistler mode chorus amplification during an injec-
403 tion event observed on CRRES, *Journal of Geophysical Research*, *113*, A09210, doi:
404 10.1029/2008JA013129.
- 405 Li, W., et al. (2009), Evaluation of whistler-mode chorus intensification on the nightside
406 during an injection event observed on the THEMIS spacecraft, *Journal of Geophysical*
407 *Research*, *114*, A00C14, doi:10.1029/2008JA013554.
- 408 Li, W., et al. (2010), THEMIS analysis of observed equatorial electron distributions re-
409 sponsible for the chorus excitation, *Journal of Geophysical Research*, *115*, A00F11,
410 doi:10.1029/2009JA014845.
- 411 Li, W., R. M. Thorne, J. Bortnik, X. Tao, and V. Angelopoulos (2012), Characteris-
412 tics of hiss-like and discrete whistler-mode emissions, *Geophysical Research Letters*, *39*,
413 L18106, doi:10.1029/2012GL053206.

- 414 Lyons, L. R., R. M. Thorne and C. F. Kennel (1971), Electron pitch-angle diffusion driven
415 by oblique whistler-mode turbulence, *Journal of Plasma Physics*, *6*, 589-606.
- 416 O'Hagan, A., and T. Leonard, Bayes Estimation subject to uncertainty about parameter
417 constraints, *Biometrika*, *63*, 201-203.
- 418 Omura, Y., Y. Katoh, and D. Summers (2008), Theory and simulation of the gener-
419 ation of whistler-mode chorus, *Journal of Geophysical Research*, *113*, A04223, doi:
420 10.1029/2007JA012622.
- 421 Shprits, Y. Y., D. M. Subbotin, N. P. Meredith and S. R. Elkington (2008), Controlling
422 effect of the pitch angle scattering rates near the edge of the loss cone on electron
423 lifetimes, *Journal of Atmospheric and Solar-Terrestrial Physics*, *70*, 1694–1713.
- 424 Su, Z., F. Xiao, H. Zheng, and S. Wang (2010), STEERB: A three-dimensional code for
425 storm-time evolution of electron radiation belt, *Journal of Geophysical Research*, *115*,
426 A09208, doi:10.1029/2009JA015210.
- 427 Thorne, R. M., S. R. Church, and D. J. Gorney (1979), Origin of plasmaspheric hiss -
428 importance of wave-propagation and the plasmopause, *Journal of Geophysical Research*,
429 *84*, 5241–5247.
- 430 Watt, C. E. J., R. Rankin, and A. W. Degeling (2012), Whistler mode wave growth
431 and propagation in the prenoon magnetosphere, *Journal of Geophysical Research*, *117*,
432 A06205, doi:10.1029/2012JA017765.

Figure 1. (a) Growing raypath from *Watt et al.* [2012] initialised at radial distance $r = 9R_E$ and magnetic latitude $\lambda = -6^\circ$. Coloured dots indicate locations with growth rates $\omega_i > 0$. The arrow indicates ray direction and the open squares indicate "observation locations". Dashed lines indicate the dipole magnetic field. (b) Growth rate as a function of distance along the raypath s . (c) Wavenormal angle as a function of s . (d) Path-integrated gain $\Gamma(a, b)$ contributions, where a is a point along s with $\omega_i > 0$, and b is the value of s at the observation location. Values are colour-coded to match the observation locations in (a).

Figure 2. (a) The raypath shown in Figure 1 traced backward from the observation location (open black square). (b) Growth rate ω_i as a function of distance along the path (where $s = 0$ indicates the observation location). The black portion of the curve indicates points along the raypath where waves can grow (i.e. $\omega_i > 0$). (c) The path-integrated gain $\Gamma(a, b)$ calculated at the observation location from each point along s with $\omega_i > 0$. The black dots indicate points along the raypath where both wave growth occurs *and* the resulting path-integrated gain is positive. These points are used to define s_0 and s_1 in equation [10]. Grey dots indicate points where the initial ω_i is positive, but the resulting gain is negative.

Figure 3. (a) The initialisation points of all contributions to wave intensity at the observation location indicated with the open black square; the colour indicates the intensity of a wave initialised from that location as it passes through the observation point. (b) Intensity at the observation point as a function of the ray direction χ for parallel waves (i.e. northward travelling waves). (c) Intensity at the observation point as a function of χ for anti-parallel waves (i.e. southward travelling waves).

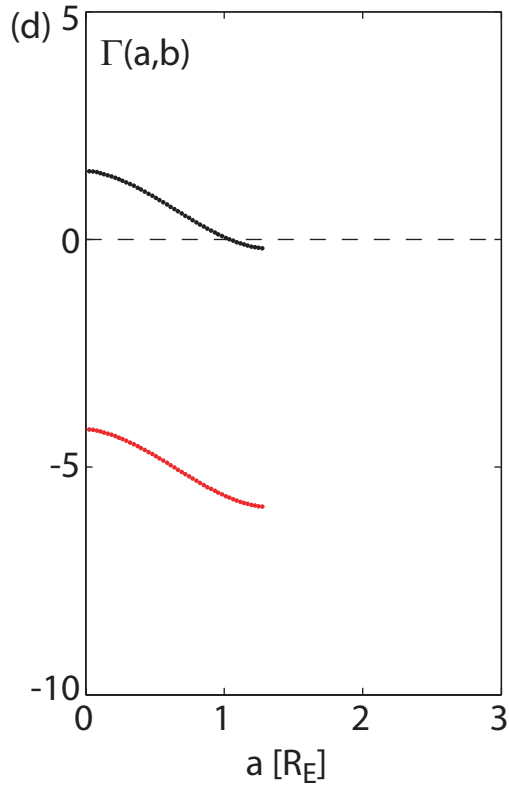
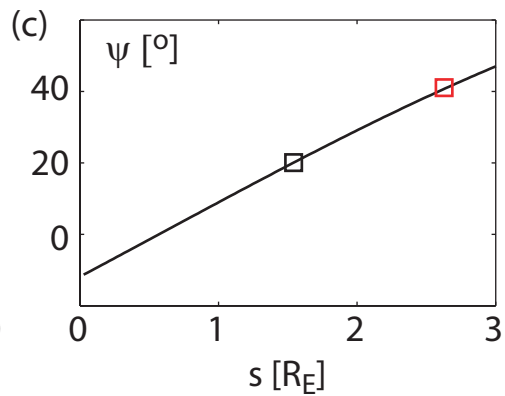
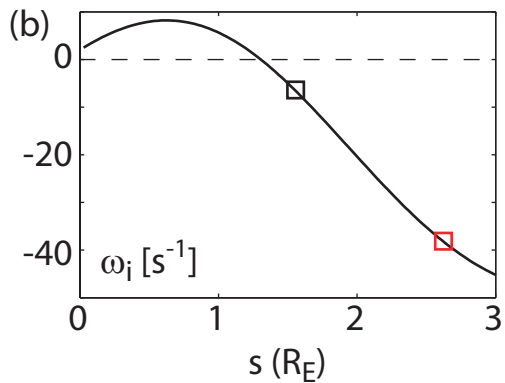
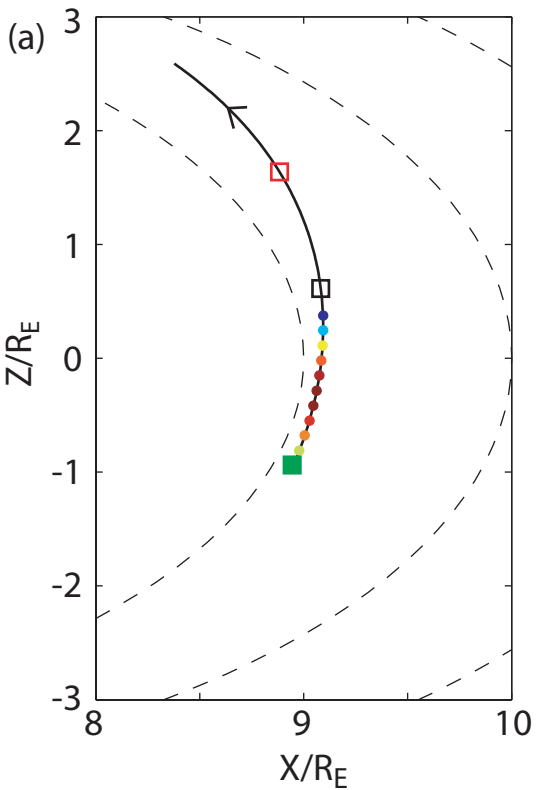
Figure 4. Wave spectral energy density as a function of frequency at $r = 9R_E$ and $\lambda = -6^\circ$. Energy density is normalised to the initial wave intensity.

Figure 5. Predicted wave spectral energy density at different latitudes at $L = 9$ for quiet time pre-noon plasma conditions (see *Watt et al.* [2012] for details of the plasma model used in this case).

Figure 6. Predicted wavenormal distributions of wave intensity at the equator at $L = 9$: (a) Near parallel and (b) near anti-parallel distributions of wave intensity as a function of normalised frequency and wavenormal angle. The white dashed lines indicate the parallel and anti-parallel magnetic field directions; (c) and (d) show cuts through the distribution at four different frequencies.

Figure 7. Predicted wavenormal distributions of wave intensity at $L = 9$ and $\lambda = 15^\circ$: (a) Near parallel and (b) near anti-parallel distributions of wave intensity as a function of normalised frequency and wavenormal angle. The white dashed lines indicate the parallel and anti-parallel magnetic field directions; (c) and (d) show cuts through the distribution at four different frequencies.

FORWARD RAYTRACING EXAMPLE



BACKWARD RAYTRACING EXAMPLE

